Interpretation of Tropical Cyclone Forecast Sensitivity from the Singular Vector Perspective

JAN-HUEY CHEN

Department of Atmospheric Sciences, National Taiwan University, Taipei, Taiwan

MELINDA S. PENG AND CAROLYN A. REYNOLDS

Naval Research Laboratory, Monterey, California

CHUN-CHIEH WU

Department of Atmospheric Sciences, National Taiwan University, Taipei, Taiwan

(Manuscript received 6 January 2009, in final form 3 June 2009)

ABSTRACT

In this study, the leading singular vectors (SVs), which are the fastest-growing perturbations (in a linear sense) to a given forecast, are used to examine and classify the dynamic relationship between tropical cyclones (TCs) and synoptic-scale environmental features that influence their evolution. Based on the 72 two-day forecasts of the 18 western North Pacific TCs in 2006, the SVs are constructed to optimize perturbation energy within a 20° × 20° latitude–longitude box centered on the 48-h forecast position of the TCs using the Navy Operational Global Atmospheric Prediction System (NOGAPS) forecast and adjoint systems. Composite techniques are employed to explore these relationships and highlight how the dominant synoptic-scale features that impact TC forecasts evolve on seasonal time scales.

The NOGAPS initial SVs show several different patterns that highlight the relationship between the TC forecast sensitivity and the environment during the western North Pacific typhoon season in 2006. In addition to the relation of the SV maximum to the inward flow region of the TC, there are three patterns identified where the local SV maxima collocate with low-radial-wind-speed regions. These regions are likely caused by the confluence of the flow associated with the TC itself and the flow from other synoptic systems, such as the subtropical high and the midlatitude jet. This is the new finding beyond the previous NOGAPS SV results on TCs. The subseasonal variations of these patterns corresponding to the dynamic characteristics are discussed. The SV total energy vertical structures for the different composites are used to demonstrate the contributions from kinetic and potential energy components of different vertical levels at initial and final times.

1. Introduction

Tropical cyclones (TCs) are one of the most destructive natural systems that cause great human and economic losses every year. Accurate predictions of both the track and the intensity of TCs are critical for disaster mitigation in areas threatened by approaching TCs. In the western North Pacific and Atlantic basins, after forming in the low latitudes under favorable environmental conditions (Gray 1975; McBride and Zehr 1981) TCs generally move westward and northwestward within the easterlies and under the influence of the beta effect (Chan and Williams 1987; Fiorino and Elsberry 1989). During their lifetime, a number of other factors also affect their track and intensity, such as the expansion or contraction of subtropical ridges (Wu et al. 2007a), approaching midlatitude troughs (Hanley et al. 2001; Peng et al. 2007; Wu et al. 2009a), the influence of vertical shear (Wu and Emanuel 1993; Wang and Wu 2004; Molinari et al. 2006), and the interaction with nearby TCs (Wu et al. 2003; Peng and Reynolds 2005; Yang et al. 2008). In the final stage, they may recurve and transition into an extratropical cyclone or make landfall and dissipate.

TC forecast inaccuracy comes both from errors in the numerical weather prediction models and from errors

Corresponding author address: Jan-Huey Chen, Dept. of Atmospheric Sciences, National Taiwan University, No. 1, Sec. 4, Roosevelt Rd., Taipei 106, Taiwan.
E-mail: cwuchen@typhoon.as.ntu.edu.tw

DOI: 10.1175/2009JAS3063.1

in the analyzed initial conditions. Concerning the latter, the lack of observations over the open-ocean regions where TCs spend most of their lifetime degrades the quality of initial conditions and the accuracy of TC forecasts (Wu 2006). Therefore, in addition to improving the forecast models, assimilating special data leads to a better TC forecast by minimizing the analysis error (Burpee et al. 1996; Aberson and Franklin 1999; Aberson 2002, 2003; Wu et al. 2007b). Singular vectors (SVs) have been used to diagnose how sensitive particular weather systems may be to small changes in the analysis and to provide guidance for targeted observation.

SVs have been used to generate initial conditions for the perturbed members of ensemble prediction systems (Molteni et al. 1996), for studies on predictability and error growth (Lorenz 1965; Farrell 1990; Molteni and Palmer 1993; Buizza 1994; Buizza and Montani 1999), and for targeted observing applications (Langland et al. 1999). Recently, SV diagnostics are used to obtain information about the dynamical processes that have an important impact on TC evolution. Peng and Reynolds (2005) used SV techniques based on the Navy Operational Global Atmospheric Prediction System (NOGAPS) to demonstrate that the analyzed position and forecast of one typhoon can have an impact on the forecast of another typhoon. Peng and Reynolds (2006) further examined the dynamics of TC motion for the Northern Hemisphere TCs in 2003 and found a distinct relationship between the NOGAPS SV sensitivity and the local potential vorticity gradient surrounding the storm. The SV sensitivity also indicated that environmental influences away from the cyclone may have a direct impact on the evolution of a storm. As to the interaction of the TC and the midlatitude system, Peng et al. (2007) demonstrated the utility of NOGAPS SVs in diagnosing complicated interactions among a midlatitude trough and three coexisting TCs in the Atlantic Ocean. Reynolds et al. (2009) used NOGAPS SVs to study the forecast sensitivity of recurving TCs in the western Pacific to changes in the initial state. Their results suggest that nonlinear forecast perturbations based on TC SVs may be useful in predicting the downstream impact of TC forecast errors over the North Pacific and North America. Kim and Jung (2008) evaluated the structure and evolution of the SVs for a recurving TC by the fifth-generation Pennsylvania State University–National Center for Atmospheric Research (NCAR) Mesoscale Model (MM5). They found that the structure of the initial SVs in the midlatitude trough region becomes dominant as the TC recurves, whereas the SV close to the TC center may be more important when the TC is far from recurvature, consistent with Peng and Reynolds (2006). It was found that the sensitive regions of the TC may evolve with the development of the storm.

In addition to the use in the field campaigns for midlatitude storms [i.e., the Fronts and Atlantic Storm-Track Experiment (FASTEX; Joly et al. 1997) and the North Pacific Experiment (NORPEX; Langland et al. 1999)], the SVs also play an important role in the targeted observing applications for TCs in both the Atlantic (Aberson 2003) and western North Pacific [i.e., the Dropwindsonde Observation for Typhoon Surveillance near the Taiwan Region (DOTSTAR; Wu et al. 2005)] regions. Majumdar et al. (2006), Reynolds et al. (2007), and Wu et al. (2009b) compared the SVs with other targeted guidance products for TCs in 2004 Atlantic season and 2006 western North Pacific season to show the similarity and the systematic structural differences among these products. Yamaguchi et al. (2009) examined the Japan Meteorological Agency (JMA) SV results and the DOTSTAR observations for the track forecast of Typhoon Conson (2004). Their results reveal that the SVs appear effective in representing the sensitive regions and would be useful for the sampling strategy of the targeted observations.

As a follow-up study to Peng and Reynolds (2006), this paper uses the 72 given 2-day forecast trajectories of the 18 TCs in 2006 to identify the relationship between the TC forecast sensitivity and the environment from the NOGAPS SV perspective. This study goes beyond the initial results of Peng and Reynolds (2006), using more specific composites that illustrate the relationship between the TC evolution and the surrounding synoptic-scale features in finer detail, and investigates the subseasonal variation of the relationship between the TC and other synoptic systems during the western North Pacific typhoon season. The dynamic relationships between the SV sensitivity and the environmental systems associated with TC evolution are interpreted. The construction of the SVs and a brief overview of TC cases in 2006 are introduced in section 2. The results of the investigations of two major SV patterns are shown in section 3. Section 4 provides the analysis of the vertical structure of the SV total energy. Section 5 is the summary and discussion.

2. Methodology and database

a. Construction of singular vectors

The leading SV represents the fastest-growing perturbation to a given trajectory (such as a weather forecast) in a linear sense (Palmer et al. 1998). Considering a nonlinear model M, acting on a state vector $\mathbf{x}$, such that $M(\mathbf{x}_0) = \mathbf{x}_t$, where the subscript refers to the integration

time, let $\mathbf{x}_0'$ represent some perturbed initial state, such that $\mathbf{x}_0' - \mathbf{x}_0 = \mathbf{p}_0$ and $M(\mathbf{x}_0') - M(\mathbf{x}_0) = \mathbf{p}_t$. For linear perturbation growth, the initial perturbation can be propagated forward in time using the forward-tangent propagator $\mathbf{L}$, representing the model equations of M linearized about the nonlinear trajectory, such that

$$\mathbf{L}\mathbf{p}_0 \cong \mathbf{p}_t. \tag{1}$$

Then $\mathbf{L}$ can be represented by its singular values and initial- and final-time SVs as

$$\mathbf{L} = \mathbf{E}^{-1/2}\mathbf{U}\mathbf{D}\mathbf{V}^{\mathrm{T}}\mathbf{E}^{1/2}, \tag{2}$$

where $\mathbf{V}$ ($\mathbf{U}$) are matrices with columns composed of the initial (final) SVs and where $\mathbf{D}$ is a diagonal matrix whose elements are the singular values of $\mathbf{L}$. Here $\mathbf{E}$ is the matrix that defines how the perturbations are measured. Thus, the SVs form an $\mathbf{E}$-orthonormal set of vectors at the initial and final times. The SVs satisfy the eigenvector equation $\mathbf{L}^{\mathrm{T}}\mathbf{E}\mathbf{L}\mathbf{y}_n = d_n^2\mathbf{E}\mathbf{y}_n$, where $\mathbf{y}_n = \mathbf{E}^{-1/2}\mathbf{v}_n$ and d_n and $\mathbf{v}_n$ are the nth singular value and initial-time SV, respectively. The leading SV maximizes the ratio of the final perturbation energy to the initial perturbation energy:

$$\frac{\langle \mathbf{L}\mathbf{p}_0; \mathbf{E}\mathbf{L}\mathbf{p}_0 \rangle}{\langle \mathbf{p}_0; \mathbf{E}\mathbf{p}_0 \rangle}, \tag{3}$$

where the angle brackets represent a Euclidean inner product. The second SV maximizes this ratio under the constraint of being orthogonal to the first SV, the third SV maximizes this ratio under the constraint of being orthogonal to the first two SVs, and so on. For complex models such as dynamical tropical cyclone models, the eigenvector equation may be solved in an iterative fashion using the forward and adjoint propagators linearized about a particular forecast.

The total-energy singular vectors (TESVs) have been computed using the tangent linear and adjoint models of NOGAPS with a total energy metric at both initial and final times (Rosmond 1997). This system contains surface drag and horizontal and vertical diffusion but does not include moist processes for those calculations. The SVs are calculated at a reduced resolution of T79L30, whereas the linearization is based on the full-physics, high-resolution (T239L30) NOGAPS forecast. The SVs employed in this study optimize the perturbation energy growth in a 20° × 20° box centered on the final-time forecast position of a TC over a 2-day optimization period using a local projection operator (Buizza 1994). The initial SVs indicate regions where the 48-h storm forecasts are most sensitive to changes in the analyses. All the SVs results discussed in section 3 are normalized by the maximum value of the vertical integration summed over the first three leading initial SVs for each case. The analysis fields from NOGAPS at 1° resolution will be used for diagnostics.

b. *Overview of the 2006 typhoon season and 72 tropical cyclone cases*

Seventy-two cases in which the Joint Typhoon Warning Center (JTWC) issued forecasts at 0000 UTC in 2006 and the storms present at 0 (initial time; t_i) and 48 (final time; t_f) hours are selected for this study (Table 1). These cases consist of forecasts for 18 different TCs (Figs. 1a,c,e,g). Multiple cases from the same storm are separated by 24 h as independent on successive days (Aberson and DeMaria 1994; Majumdar et al. 2006; Wu et al. 2009b; Reynolds et al. 2009). The verification area for the NOGAPS TESV calculation is chosen to be centered at the 48-h (t_f) TC position forecasted by the JTWC. The inspection of final SVs is used to make sure that the initial SVs are related to the storm and not to some independent feature. Because there is no other major weather system within the verification domain, the final SV corresponds to the final state of that storm. The SV sensitivities of all 72 cases have been examined and confirmed to be storm related. The details of the verification area and the model initial and final times for each case are listed in Table 1.

Figure 1 shows the tracks of the 18 TCs and their corresponding synoptic average height at 500 hPa and the pressure-weighted deep-layer-mean wind from 850 to 300 hPa fields from the NOGAPS analysis. The 18 TCs are divided into four periods (May–June, July–August, September–October, and November–December) in 2006 to show the subseasonal variation of the TC movements and the synoptic environment in the western North Pacific. Typhoon Chanchu is the only TC in the early typhoon season (May) (Fig. 1a). The height and deep-layer-mean wind fields of the seven cases of Chanchu (cases 1–7 in Table 1) at their initial time are averaged to show the synoptic environment during this period. Typhoon Chanchu moved westward and then turned to the north when it moved to the South China Sea (Fig. 1a). The average deep-layer-mean wind field from 850 to 300 hPa shows the consistent flow direction with Chanchu's movement, mainly associated with the circulation of subtropical high around 20–30°N, 125–140°E [indicated by 5880 geopotential meters (gpm) with the black bold line in Fig. 1b]. During the middle typhoon season (July and August), 30 cases occurred that corresponded to eight TCs. Besides Typhoon Ioke, the other seven TCs are generated to the west of 140°E (Fig. 1c). The average height field shows a stronger

TABLE 1. Summary of 72 cases in 2006. Except for Typhoon Ioke, all annual numbers are for the West Pacific Basin. All initial time (t_i) and final time (t_f) are from 0000 UTC; for example, 0511 = 0000 UTC 11 May 2006. The northern and southern (°N) and western and eastern (°E) periphery of the rectangular verifying area centered on the JTWC 48-h forecast position of the TC valid at the verifying time is listed. The JTWC analysis of the storm intensity (kt) at the initial time is also listed. The classification base on the collocation of SV maximum and the radial wind field at 500 hPa for each case (see section 3) is listed in the last column.

No.	Annual number and name	t_i	t_f	Verifying area (centered on the 48-h forecast position of the TC) °N	°S	°W	°E	Intensity (kt) at t_i	Classification
1	02W Chanchu	0511	0513	3.7	23.7	112.9	132.9	75	A
2	02W Chanchu	0512	0514	5.2	25.2	107.0	127.0	65	A
3	02W Chanchu	0513	0515	5.0	25.0	105.7	125.7	75	A
4	02W Chanchu	0514	0516	7.0	27.0	104.3	124.3	90	A
5	02W Chanchu	0515	0517	9.8	29.8	104.2	124.2	135	NI
6	02W Chanchu	0516	0518	15.1	35.1	107.0	127.0	115	RI
7	02W Chanchu	0517	0519	19.9	39.9	112.1	132.1	100	RI
8	04W Ewiniar	0703	0705	6.7	26.7	120.5	140.5	65	B
9	04W Ewiniar	0704	0706	9.3	29.3	119.0	139.0	100	B
10	04W Ewiniar	0705	0707	12.4	32.4	119.0	139.0	130	C
11	04W Ewiniar	0706	0708	15.0	35.0	117.2	137.2	105	C
12	04W Ewiniar	0707	0709	18.4	38.4	115.7	135.7	100	C
13	04W Ewiniar	0708	0710	22.4	42.4	114.9	134.9	85	NI
14	04W Ewiniar	0709	0711	29.8	49.8	116.0	136.0	75	RI
15	05W Bilis	0712	0714	16.2	36.2	110.2	130.2	45	B
16	05W Bilis	0713	0715	17.2	37.2	108.3	128.3	50	A
17	06W Kaemi	0721	0723	10.4	30.4	116.6	136.6	85	NI
18	06W Kaemi	0722	0724	10.3	30.3	112.9	132.9	90	NI
19	06W Kaemi	0723	0725	13.5	33.5	111.9	131.9	85	NI
20	06W Kaemi	0724	0726	14.1	34.1	106.8	126.8	65	B
21	08W Saomai	0808	0810	16.2	36.2	112.1	132.1	75	A
22	08W Saomai	0809	0811	16.7	36.7	106.0	126.0	105	NI
23	09W Maria	0808	0810	26.6	46.6	127.4	147.4	55	RI
24	10W Bopha	0809	0811	11.9	31.9	104.7	124.7	35	NI
25	11W Wukong	0815	0817	20.5	40.5	125.1	145.1	50	C
26	11W Wukong	0816	0818	20.9	40.9	120.0	140.0	45	RI
27	11W Wukong	0817	0819	24.9	44.9	118.5	138.5	45	RI
28	14W Shanshan	0913	0915	11.8	31.8	115.7	135.7	90	A
29	14W Shanshan	0914	0916	14.2	34.2	113.7	133.7	75	NI
30	14W Shanshan	0915	0917	19.9	39.9	116.7	136.7	100	NI
31	14W Shanshan	0916	0918	26.4	46.4	121.2	141.2	120	RI
32	16W Yagi	0920	0922	12.9	32.9	134.9	154.9	115	NI
33	16W Yagi	0921	0923	16.4	36.4	131.1	151.1	120	RI
34	16W Yagi	0922	0924	23.5	43.5	134.1	154.1	140	RI
35	18W Xangsane	0928	0930	6.0	26.0	102.8	122.8	105	NI
36	18W Xangsane	0929	1001	5.6	25.6	98.4	118.4	100	A
37	19W Bebinca	1005	1007	17.3	37.3	126.0	146.0	45	RI
38	21W Soulik	1012	1014	14.0	34.0	129.1	149.1	60	C
39	21W Soulik	1013	1015	15.6	35.6	129.8	149.8	75	RI
40	21W Soulik	1014	1016	21.1	41.1	135.5	155.5	90	RI
41	22W Cimaron	1029	1031	7.6	27.6	107.9	127.9	120	C
42	22W Cimaron	1030	1101	7.1	27.1	103.9	123.9	95	C
43	22W Cimaron	1031	1102	8.2	28.2	102.0	122.0	90	NI
44	22W Cimaron	1101	1103	11.2	31.2	103.1	123.1	100	RI
45	22W Cimaron	1102	1104	10.0	30.0	107.4	127.4	95	RI
46	23W Chebi	1112	1114	6.8	26.8	100.5	120.5	75	C
47	23W Chebi	1113	1115	8.5	28.5	99.6	119.6	60	RI
48	23W Chebi	1114	1116	10.0	30.0	98.1	118.1	35	RI
49	24W Durian	1128	1130	4.8	24.8	115.5	135.5	55	C
50	24W Durian	1129	1201	5.3	25.3	111.3	131.3	90	C
51	24W Durian	1130	1202	4.8	24.8	108.4	128.4	135	RI
52	24W Durian	1201	1203	3.7	23.7	103.2	123.2	95	C
53	24W Durian	1202	1204	2.9	22.9	101.0	121.0	75	C
54	24W Durian	1203	1205	1.8	21.8	98.3	118.3	90	RI

TABLE 1. (*Continued*)

No.	Annual number and name	t_i	t_f	Verifying area (centered on the 48-h forecast position of the TC) °N	°S	°W	°E	Intensity (kt) at t_i	Classification
55	25W Utor	1210	1212	3.9	23.9	104.3	124.3	100	C
56	25W Utor	1211	1213	5.1	25.1	103.1	123.1	75	C
57	25W Utor	1212	1214	7.0	27.0	101.3	121.3	75	B
58	25W Utor	1213	1215	7.7	27.7	101.1	121.1	95	RI
59	01C Ioke	0822	0824	8.4	28.4	177.8	197.8	115	NI
60	01C Ioke	0823	0825	9.7	29.7	175.8	195.8	90	A
61	01C Ioke	0824	0826	10.0	30.0	173.7	193.7	90	A
62	01C Ioke	0825	0827	9.5	29.5	171.1	191.1	125	NI
63	01C Ioke	0826	0828	8.1	28.1	168.2	188.2	130	NI
64	01C Ioke	0827	0829	7.3	27.3	163.2	183.2	140	A
65	01C Ioke	0828	0830	7.4	27.4	160.5	180.5	135	NI
66	01C Ioke	0829	0831	9.2	29.2	157.6	177.6	130	NI
67	01C Ioke	0830	0901	10.6	30.6	154.5	174.5	140	NI
68	01C Ioke	0831	0902	11.9	31.9	149.8	169.8	135	A
69	01C Ioke	0901	0903	14.2	34.2	144.8	164.8	130	NI
70	01C Ioke	0902	0904	16.7	36.7	140.0	160.0	115	NI
71	01C Ioke	0903	0905	21.6	41.6	135.5	155.5	100	NI
72	01C Ioke	0904	0906	30.7	50.7	140.4	160.4	85	RI

subtropical high than in the previous period (cf. Figs. 1b,d). The average deep-layer-mean wind field from 850 to 300 hPa demonstrates that the large-scale easterly flow along the southern edge of the subtropical high becomes southeasterly when it crosses 160°E. The movements of Typhoon Ioke and other seven TCs follow the synoptic flow and show northwestward tracks (Fig. 1c).

In autumn (September and October) of 2006, half of the TCs show recurving tracks (Fig. 1e). Compared with Fig. 1d, Fig. 1f shows a weaker subtropical high accompanied with denser isohypse and stronger wind in the midlatitude area. It illustrates that these TCs are often affected by the midlatitude systems and then recurve to the north during this period. In the late typhoon season (November and December), four TCs develop near the Philippines and move toward the west (Fig. 1g). The 5880-gpm contour covers a broad area, extending from 120° to 175°E in low latitudes (Fig. 1h). It appears that the flow associated with the southwestern edge of the subtropical high steered the TCs westward.

From the above analysis, it can be found that the TC tracks are linked to environmental large-scale systems such as the subtropical high and the midlatitude trough or jet. It agrees with the well-known concept that the TC movement is mainly driven by the steering flow. Moreover, in the western North Pacific, the environmental flow is dominated by the large-scale circulation, which is generally related to the Asian monsoon or the strength and the location of the subtropical high. The seasonal variation of this large-scale circulation results in the change of the steering flow. Therefore, the TCs show different tracks in different periods of the typhoon season in 2006.

3. Results of the two major SV patterns in 2006

Composites for the total 72 cases are made of the initial SV and the radial wind field (U_r) with respect to the center of the storm from the NOGAPS analysis at 500 hPa (Fig. 2a). For each case, a 100° × 100° latitude–longitude area centered on the storm center at the initial time is adopted to construct the composites. Figure 2a shows that the initial SV is collocated with the inflow region (the area with the negative speed of U_r) and the maximum SV is located at around 500 km from the center. In this study, the terms ''inflow'' or ''inward flow'' indicate the (negative) radial component of the wind flow relative to the storm center moving toward the storm but do not necessarily denote the flow associated with the storm itself. It agrees well with the findings of Peng and Reynolds (2006) that the initial SV sensitivity exhibits a maximum at approximately 500 km from the storm center and the maximum areas are associated with the inflow regions. Peng and Reynolds (2006) also found that the sensitivity was in the right-rear quadrant of the storms by compositing the initial SV with respect to the storm center and rotating it based on storm direction. Individual cases have been examined in this study and it is found that the relation between the moving direction and the location of maximum initial SV in general agrees with the findings in Peng and Reynolds (2006).

Figure 2b is the composite of the height field at 500 hPa and the pressure-weighted deep-layer-mean wind field from 850 to 300 hPa relative to the storm center of each case in Fig. 2a. The TC development depth related to its intensity is the main factor in the

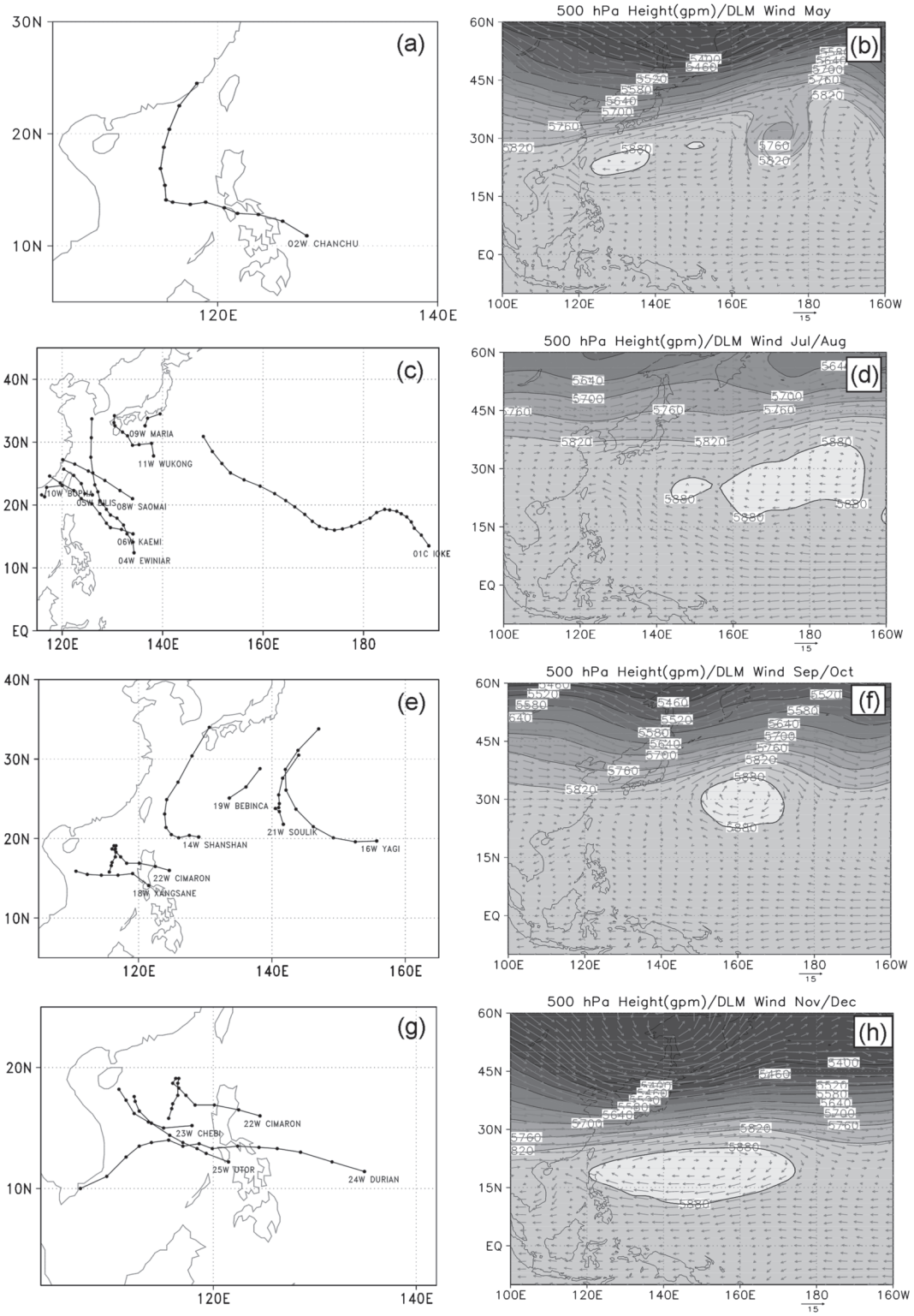

FIG. 1. (a),(c),(e),(g) The JTWC best tracks of the 18 TCs and (b),(d),(f),(h) their corresponding 500-hPa height (contour and shaded) and the deep-layer-mean wind (vector) average synoptic fields at the initial time from the NOGAPS analysis. The name and annual cyclone number of the TC are marked in the beginning of each track. Each symbol is plotted at 12-h intervals. The scales of the composited height and wind fields are indicated by the label of the contour (gpm) and the arrow to the lower right (m s^{-1}). The bold lines in (b),(d),(f), and (h) show the height at 5880 gpm.

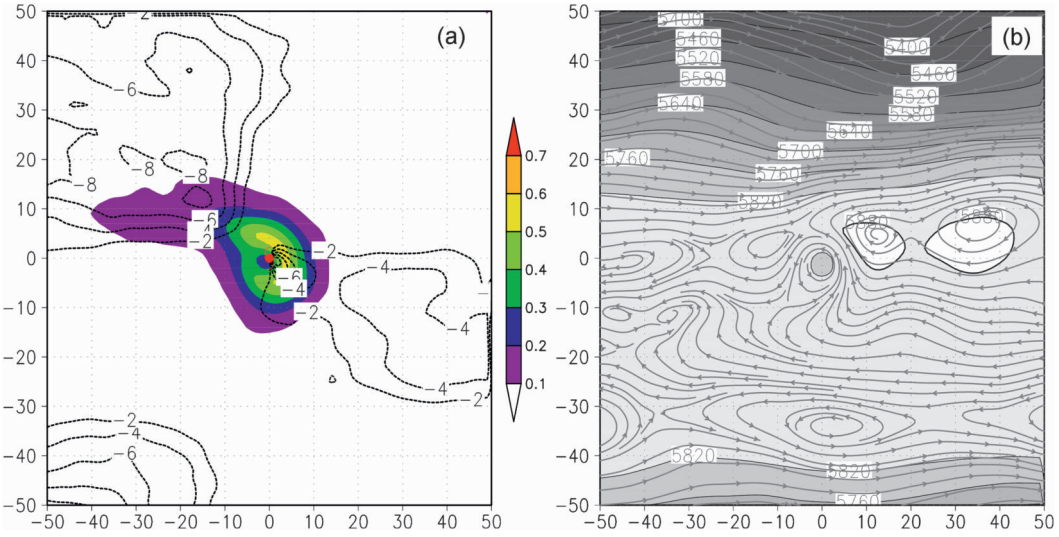

FIG. 2. 72-case composites of (a) the initial SVs (colors) and the radial wind (contours, negative values only; m s^{-1}), and (b) the height (shading and contours; gpm) at 500 hPa and the deep-layer-mean wind (streamlines) fields at the initial time. The TC symbol in (a) indicates the composited TC center. The bold line in (b) marks the height at 5880 gpm.

choice of the deep-layer-mean wind layers (Velden and Leslie 1991; Wu et al. 2003; Yang et al. 2008). Considering the diversity of the TC intensity among cases, 850–300 hPa is adopted as the intermediate layer for the deep-layer-mean wind composite in this study. Note that there are two major synoptic systems around the TC. One is the subtropical high to the eastern side of the storm indicated by the contour of 5880 gpm (bold contour) and the other is the midlatitude trough or jet located to the north of the storm. Comparison of Figs. 2a and 2b shows that the inflow region to the southeast side of the storm is associated with circulation around the subtropical high, while the other inflow region located in the northwest quadrant is associated with the midlatitude system. Both of the systems appear to affect the TC evolution.

Examination of the individual cases indicates that the SV maximum is collocated with flow toward the storm center, consistent with Peng and Reynolds (2006) in several, but not all, of the cases. In an effort to understand the dynamics associated with various types of situations, the SVs are first classified into two major groups according to their characteristics. The first group is composed of cases in which the SV maximum is collocated with the ''strong'' inflow region (where U_r is at its negative maximum). The second group is composed of cases in which the SV maxima are collocated with the regions where the corresponded U_r is not the local maximum. Examination of the first group indicates that the inward flow cases can be further stratified into 21 ''near inflow'' (NI) cases and 20 ''remote inflow'' (RI) cases based on the distance between the SV maximum and the TC center. This first group is examined in detail in section 3a. Examination of the second group indicates that when the SVs are not collocated with maximum inward flow, they are collocated with the low-radial-wind-speed area. Some of these low-radial-wind-speed areas are within the ''weak'' inflow region (with negative U_r, but not local negative maximum), and others are located between the inflow and outflow regions, where U_r is close to zero. This is a new finding and will be discussed in detail in section 3b, where the 31 low-radial-wind-speed cases are further classified into three different subgroups based on their orientation relative to the TC center.

a. Inward flow group

In this group, the SV maximum is collocated with the strong inflow region where U_r is a negative maximum. Based on the distance between the SV maximum and TC center, this group is further divided into two subgroups. Figure 3 shows the composites of initial SVs and radial wind field of 21 near-inflow (NI) and 20 remote-inflow (RI) cases centered on the storm. The SV maximum for the NI composite (Fig. 3a) is located in the inflow region to the east of the storm and is very close to the storm center. The distance between the SV maximum and the storm center is around 450 km where the average radial wind speed is about 8–10 m s^{-1}. The location of the SV maximum and the maximum inward flow are highly correlated. In contrast to a single SV maximum in the NI composite, the SV maxima of the RI composite typically occur in two places (Fig. 3b). The primary maximum is associated with regions of inward

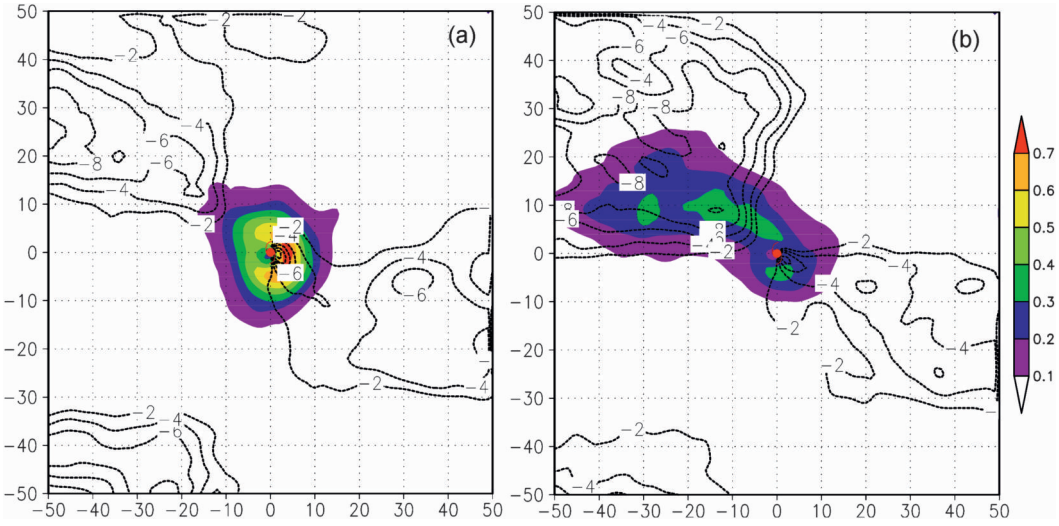

FIG. 3. Composites of the initial SVs (colors) and the radial wind (contours, negative values only; m s^{-1}) at 500 hPa at the initial time for the (a) NI and (b) RI groups. The TC symbols indicate the composited TC center.

flow located in the northwestern quadrant of the storm center where the radial wind speed is about 8–10 m s^{-1}. Compared with the NI cases, the distance between the primary SV maximum and the storm center is much larger (1500–2000 km). The secondary SV maximum of the RI composite occurs to the south of the storm center. Similar to the NI composite, this maximum is more associated with inward flow in the southeast quadrant.

The monthly statistics of the case numbers for the two inward flow subgroups can be found in Table 2. It shows an interesting seasonal distribution: most of the NI cases happen earlier in the typhoon season (July to September) whereas the number of the RI cases peaks later in the season. Almost 70% of the NI cases happen in August and September (15 of total 21 NI cases), and these NI cases account for half the total number (15 of 30 cases) in the two months. In contrast, about 35% of the RI cases occur in the very late season (November and December). These RI cases account for 46% of the cases in November and December, whereas there is no NI case during this period. Compared to the NI group, the monthly distribution of RI case number is more uniform. Moreover, looking into the eight TCs (Chanchu, Ewiniar, Kaemi, Shanshan, Cimaron, Durian, Utor, and Ioke) with a lifetime longer than 4 days in this study, it can be found that the RI pattern usually shows up in their late development stage, except for the case of Kaemi (Table 1). These seven TCs occurred in different subseasons of 2006, indicating that in addition to the seasonal characteristics, the occurrence of RI pattern is also related to the TC development stage.

The locations of the individual initial SV maxima and the TC centers for the NI and RI cases are shown in Fig. 4. Most of the NI SV maxima and TC centers are located over the open ocean. In contrast, more than half of the RI SV maxima occur over the Asian continent around 30°–50°N while the TC centers are located close to the coast. The composites of synoptic fields centered on the storm (Fig. 5) illustrate that the locations of the subtropical high and midlatitude jet are different for the NI and RI cases. Figure 5a shows that the subtropical high (approximately indicated by the 5880 gpm bold contour) is to the northeast of the TC for the NI cases, whereas it is located to the east side of the TC for the RI cases (Fig. 5b). Analyses of the height fields to the north of the TC show that the 5820-gpm contour is closer to the storm in the RI cases (about 10° north of the TC center in Fig. 5b) than in the NI cases (about 17° north of the TC center in Fig. 5a). This is because the overall subtropical high system in the NI cases extends to the west and north of the TCs and in a way blocks the effect of the midlatitude systems on the TCs. In addition, the westerly wind belt to the north of the storm is closer to the TC center in the RI cases (Fig. 5b) than in the NI cases (Fig. 5a). The above two results suggest that the

TABLE 2. Monthly distribution of case numbers for the NI, RI, A, B, and C groups and the subtotal in each month.

Group	May	Jul	Aug	Sep	Oct	Nov	Dec	Total
NI	1	4	8	7	1	0	0	21
RI	2	1	3	4	3	5	2	20
A	4	1	5	2	0	0	0	12
B	0	4	0	0	0	0	1	5
C	0	3	1	0	3	3	4	14
Total	7	13	17	13	7	8	7	72

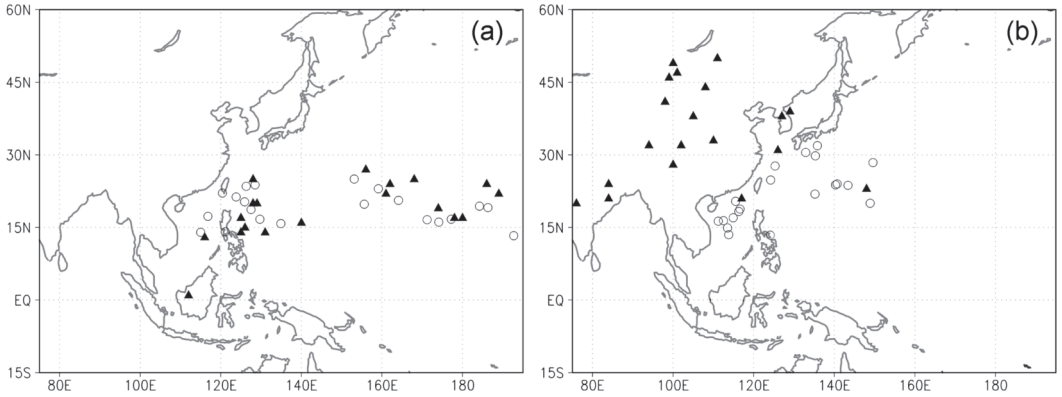

FIG. 4. The locations of initial SV maximum (▲) and the TC center (○) at the initial time for each (a) NI and (b) RI case.

midlatitude systems (jet or trough) are in closer proximity to the TC for the RI cases than for the NI cases, while the subtropical high system lies to the north and west of TCs in the NI cases.

In summary, most of the NI cases occur in the early typhoon season when the subtropical high circulation extends to the west and steers the TCs to the west or west-northwest. For these cases, the SV sensitivities are located to the east of the TCs. This is consistent with Peng and Reynolds (2006), in which the maximum SV is located to the right-rear quadrant for straight-moving storms. Most of the RI cases, on the other hand, occur in the late typhoon season or late TC development stage when the subtropical high is located to the east, and TCs in this group recurve under the influence of the both the subtropical high and a midlatitude jet or trough. Therefore, the primary SV maxima show higher sensitivities to the midlatitude systems to the northwest of the TCs and farther away from the storm centers, while the secondary SV maxima occur to the south of the storms. Many studies, such as Elsberry (1986), Chan and Gray (1982), and Wu and Emanuel (1995a,b), demonstrated that the steering flow is an important factor in TC movement. The radial component of the wind field used in this study represents the steering flow qualitatively. It is believed that the SV sensitivity marks the region where the change of inward flow will influence the future track of the TC.

b. Low-radial-wind-speed group

In this group, 31 cases in which the SVs are not collocated with the strong inflow area (U_r at its negative maximum) are studied. Examination of these cases indicated that their SVs are within low-radial-wind-speed area. Some of these low-radial-wind-speed areas are within the weak inflow region (with negative U_r, but its absolute value and not the local maximum) and others are located between the inflow and outflow regions, where U_r is close to zero. It is a new and interesting finding. These low-radial-wind-speed cases can be divided into three subgroups (A, B, and C) based on the locations of the SV maxima relative to the storm centers. In group A (12 cases), the SV maxima are mainly located to the east of the TC (Fig. 6a), whereas the SV maxima are located to the southeast and northwest of the TC in groups B (5 cases) and C (14 cases), respectively (Figs. 6b,c).

Figure 6 shows the composited SV maxima and the composited radial wind fields centered on the storm for the three subgroups. The positive values of the radial wind are also shown in Fig. 6 to demonstrate that the SV maxima are collocated with the low-radial-wind-speed areas. From Fig. 6a, the composite of group A shows that the SV maximum is located to the east of the TC center and is collocated with the inflow region, similar to the characteristics of the NI cases (Fig. 3a). However, the radial wind speed in the SV maximum region is around 4–6 m s^{-1} in group A, which is lower than that in group NI (8–10 m s^{-1}). For group B, the SV maximum shifts to the southeast side of the TC center (Fig. 6b). The SV maximum again occurs in a negative radial wind (inflow) region with speeds of about 4 m s^{-1}. In group C, the SV maximum occurs in the northwestern quadrant of TC center (Fig. 6c). Figure 6c clearly shows that the SV maximum is located between the inflow and outflow region where the radial wind speed is lower than 3 m s^{-1}. Moreover, it can be noted that the pattern of the initial SV maximum in group C is revealed to the northwest side of the storm and appears to be more associated with the inflow region in the same quadrant.

To further investigate the low-radial-wind-speed regimes, the streamlines of the composited pressure-weighted deep-layer-mean wind fields from 850 to 300 hPa centered on the storm in a domain size smaller

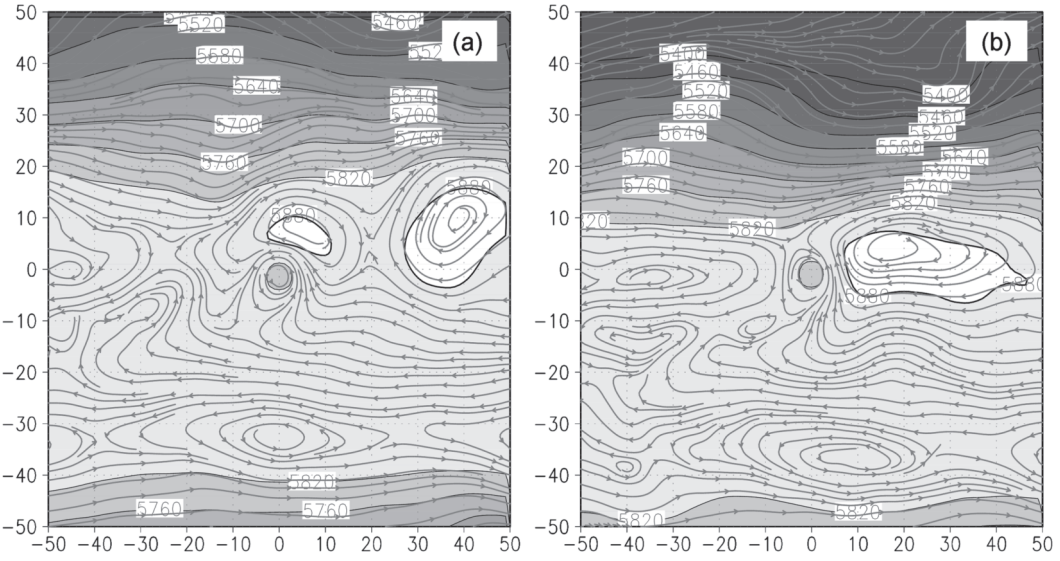

FIG. 5. Composites of the 500-hPa height (shading and contours; gpm) and the deep-layer-mean wind (streamlines) fields centered on the storm at the initial time for the (a) NI and (b) RI groups. The bold lines mark the height at 5880 gpm.

than that in Fig. 6 are used to represent the synoptic systems surrounding the TCs (Figs. 7a–c). The relations of these synoptic systems to the low-radial-wind-speed areas can be revealed for the three subgroups. A schematic diagram is also shown in Figs. 7d–f to illustrate the location of the storm relative to the surrounding synoptic systems, such as the subtropical high and the midlatitude jet, and the suggested low-radial-wind-speed regions. In Figs. 7a and 7d, it can be seen that the low-radial-wind-speed area to the east of the TC in group A is induced by the confluence of circulations associated with both the subtropical high and the TC itself. At the confluence area (indicated by the star in Fig. 7d), the southeasterly flow from the subtropical high and the southwesterly flow from the TC circulation cause the reduction of the zonal component of the wind locally while enhancing the southerly component of wind to the east of the TC. Because of the weak zonal wind, the radial wind speed is low in the region that is to the east side of the storm center (Fig. 6a). In Fig. 7b, the composited wind field shows that the circulation of the subtropical high is expanded to the east of the TC in group B. Therefore, the confluence of the subtropical high and the TC circulation shifts to the southeast side of the storm center (Figs. 7b,e). The easterly flow to the east of the star in Fig. 7e is associated with the subtropical high, while the westerly flow on west side is associated with the counterclockwise circulation of the TC. The counteraction of the flows from the two systems causes the weak wind in the confluence region and thus the low speed of the radial wind as shown in Fig. 6b. For group C, the situation is different and more complicated. Figure 7c shows that the SV maximum is located at a saddle located to the northwest of the storm. This saddle is caused by the confluence of the circulations from four systems: the subtropical high, the midlatitude jet, the TC, and a separated high located to the west (Fig. 7f). The wind speed is low at the saddle, and the radial wind speed is consequently low (Fig. 6c).

The monthly statistics of case numbers for the three low-radial-wind-speed subgroups are listed in Table 2. Seasonal differences are found among the three subgroups. Over 80% of group-A cases occur in the early season (May, July, and August). In contrast, 71% of group-C cases occur in the late season (October–December) and the remaining 4 cases (29% of group-C cases) are in July and August. Moreover, group-C cases account for 45% of the cases (10 of 22 cases) in October to December but just 13% (4 of 30 cases) in July and August. Of the five group-B cases, four occur in the early season (July) but the last happens quite late (in December). It can be found that continuity or serial correlation also plays a role in the results. For example, the first four cases in Typhoon Chauchu show a group-A pattern continually. It is reasonable because the synoptic environment will not often show sudden changes within several days.

Figure 8 shows the synoptic patterns associated with the three subgroups through composites of the geopotential heights and streamlines centered on the storm in a broader region than in Fig. 7. The location of subtropical high is to the north of the TC in group A (Fig. 8a). The subtropical high resides to the east and northeast of

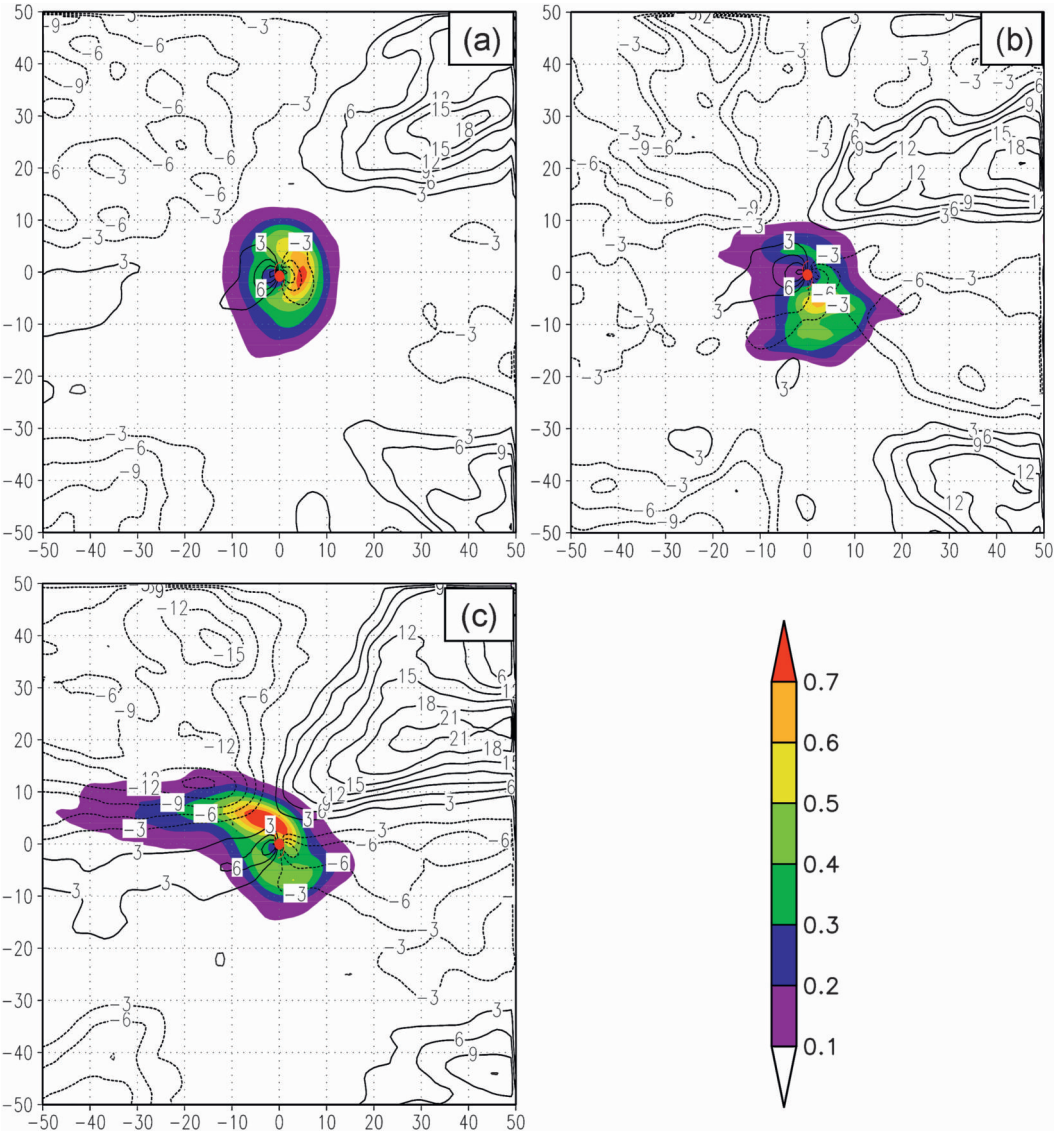

FIG. 6. Composites of the initial SVs (colors) and the radial wind (contours; m s^{-1}) at 500 hPa at the initial time for the (a) A, (b) B, and (c) C groups. The TC symbols indicate the composited TC center.

the TC in groups B and C (Figs. 8b,c). Based on the contour of 5880 gpm, the range of the subtropical high in group A is the smallest (covering 17 longitudinal degrees to the north of the TC; Fig. 8a) and it is broader in groups B and C (covering more than 50 longitudinal degrees to the east of the TC; Figs. 8b,c). In group A, the westerly belt in the midlatitude is far to the north of the TC (Fig. 8a). In contrast, the position of the midlatitude jet is much closer to the TC (around 10° north of the TC center) in group C (Fig. 8c). The wind field also shows that the westerly wind belt in group C is more zonal and occurs in a broader latitudinal area than in groups A and B.

The correlation between the SV sensitivity and a low-radial-wind-speed region leads us to examine the surrounding synoptic systems and their subseasonal variations. In the early typhoon season, the SV maxima occur in the low-radial-wind-speed region caused by the confluence of the circulations from the subtropical high and the TC, such as the group-A cases. Starting from July, the subtropical high becomes stronger and extends its range to 50 longitudinal degrees (cf. Figs. 8a,b). Thus, some of the confluence regions are shown at the southeast quadrant of the TC (e.g., the four group-B cases in July). As the season evolves, the midlatitude systems move to lower latitudes and start to influence the TC evolution. Several major systems, such as the subtropical high, the midlatitude jet, the TC, and the separated high located to the west, result in the confluent flows at the

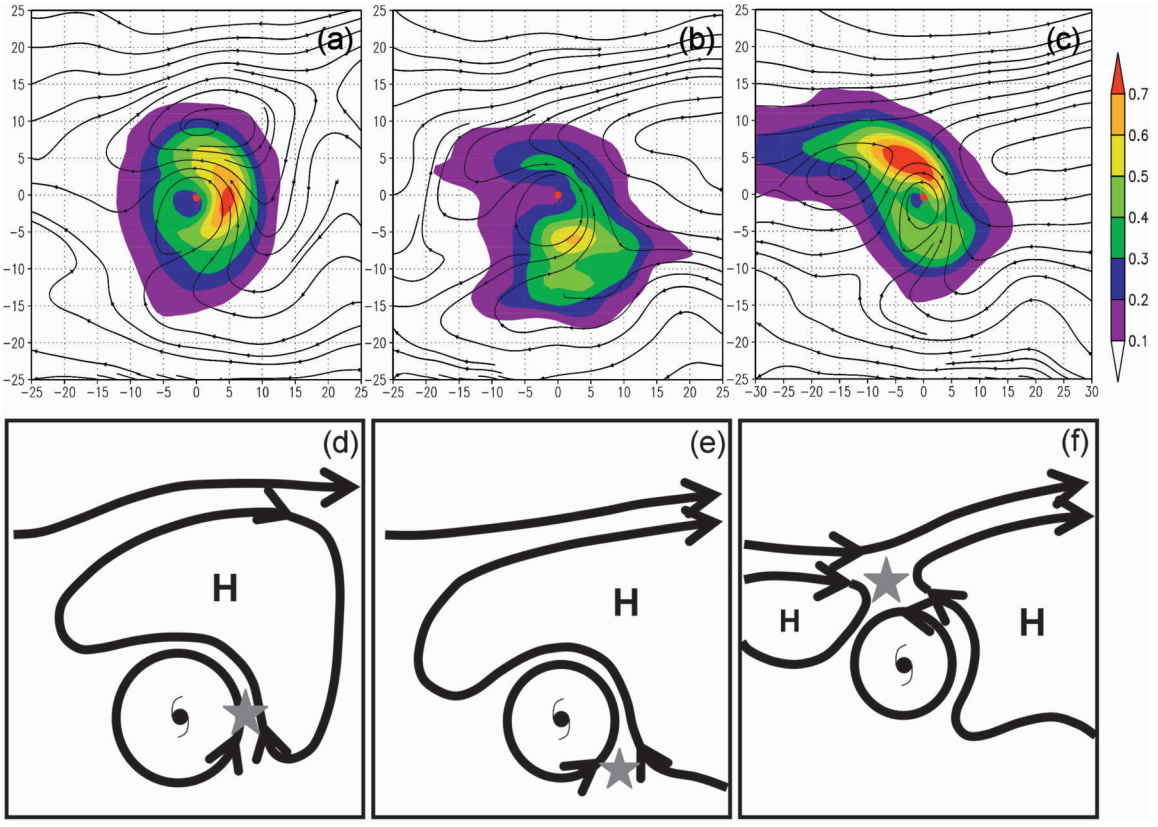

FIG. 7. (a)–(c) Composites of the initial SVs (colors) and the deep-layer-mean wind field (streamlines) at the initial time for subgroups (a) A, (b) B, and (c) C of the low-radial-wind-speed group, and (d)–(f) the corresponding schematics of these three subgroups. In (a)–(c), the red typhoon symbols represent the storm center, and the domain size is smaller than that in Fig. 6 to show more details close to the storm center. In (d)–(f), "H" and typhoon symbols represent the subtropical high and the TC, respectively. The direction and the range of the circulation of these two systems and the location of midlatitude jet flow are shown by the lines with the arrowhead.

same time and form the clear saddle pattern and the low-radial-wind-speed regime. Therefore, the low-radial-wind-speed region shifts to the northwest side of the TC in the late typhoon season. The SV maxima of most of the group-C cases are collocated with these low-radial-wind-speed regions at this time.

As mentioned before, the steering flow is the dominant factor controlling the TC movement (Elsberry 1986; Chan and Gray 1982; Wu and Emanuel 1995a,b). At the confluence area, especially the saddle point, the steering flow is usually weak and results in difficult TC track forecasting in both subjective and numerical forecasts. In this research, the initial SV maxima often occur in the confluence regions between several systems, such as the subtropical high, the midlatitude jet, and the TC itself. Meanwhile, the subseasonal correlation of the changes of the low-speed radial wind and the SV maximum are found in the monthly distribution and synoptic analysis. The low-radial-wind-speed areas represent regions with a delicate balance between two or more synoptic systems. A small perturbation locally can be the result of more significant differences of the associated synoptic systems that could lead to very different steering flow and impact the TC evolution.

c. *TC intensity and the five subgroups*

In addition to the monthly case-number distribution and the synoptic analysis, the correlation of the TC intensity and the five subgroups (NI, RI, A, B, and C) are also examined. According to the Saffir–Simpson scale, based on the JTWC analysis of the storm intensity at the initial time (see Table 1), the 72 cases are divided into 30 major typhoons (MTY; maximum sustained wind $>$ 96 kt; i.e., category 3 and above), 30 typhoons (TY; 64–96 kt; categories 1 and 2), and 12 tropical storms (TS; $<$ 64 kt). The case numbers of the five subgroups for the three intensity categories are listed in Table 3. For the 30 MTY cases, 70% of the cases have their SV maxima at the inflow region while 30% occur at the low-radial-wind-speed region. Almost 50% of the cases in this category are in the NI group. The situation is different in the 30-case TY category. More cases show their SV

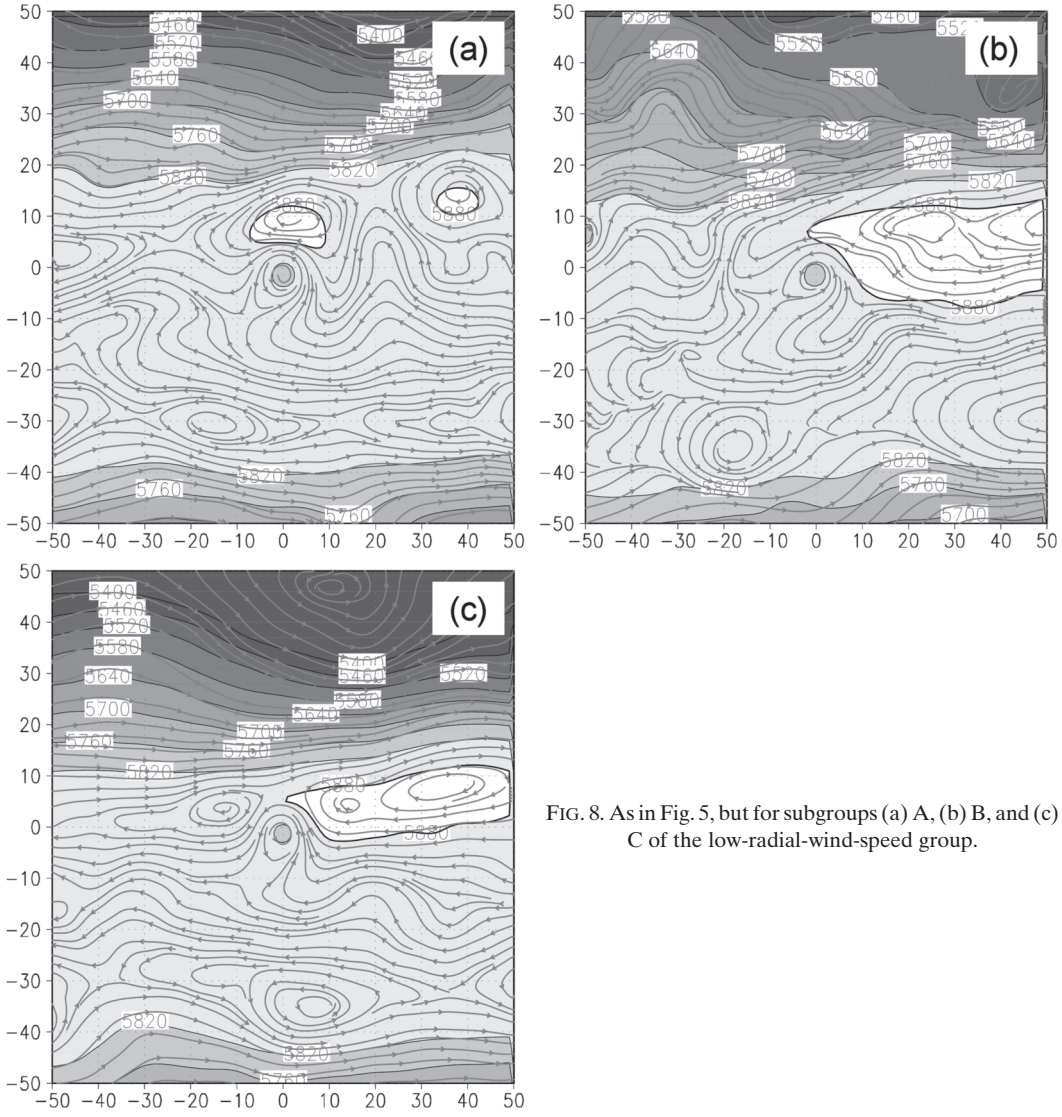

FIG. 8. As in Fig. 5, but for subgroups (a) A, (b) B, and (c) C of the low-radial-wind-speed group.

maxima at the low-radial-wind-speed region (57%) than at the inward flow region (43%). Group A contains the largest number of the TY cases (27%). However, the case numbers of the NI, RI, A, and C groups are rather close in the TY category. Of the 12 TS cases, most show their SV maxima at the remote inflow region (50%); however, 25% are in group C.

To interpret the above results, we compare our findings with the TC motion theory as reviewed in Elsberry (1986), which indicated that the total flow system contains not only the axially symmetric circulation associated with the vortex and the large-scale environmental flow (steering flow) but also the asymmetric circulation from the interaction between the symmetric circulation and the environment. Chan and Gray (1982) studied the dependence of motion on TC structure and found that systematic difference between the steering flow vector and the storm motion vector as a function of cyclone size and intensity. They used ''directional difference'' (''DD'') to show the difference between the direction of the surrounding wind and that of the cyclone. The increases in the DD are found to correlate very well with the increases in cyclone intensity and size. From the results of Chan and Gray (1982) and the correlation of the TC intensity and the five SV subgroups discussed in the above paragraphs, we propose an interpretation that strong storms may be less influenced by surrounding systems and thus tend to have more straight-moving tracks. Therefore, MTY cases fall more into the NI group. In contrast, more cases occur in the RI group as weak storms, which are more prone to the influence of the environment.

TABLE 3. Case numbers (upper) and the corresponding percentage (lower) for the inward flow (NI and RI) and low-radial-wind-speed (A, B, and C) groups for three TC intensity categories (major typhoon, typhoon, and tropical storm).

	Inward flow		Low-radial-speed wind			
Group	NI	RI	A	B	C	Total
Major typhoon	14	7	3	1	5	30
	47%	23%	10%	3%	17%	100%
Typhoon	6	7	8	3	6	30
	20%	23%	27%	10%	20%	100%
Tropical storm	1	6	1	1	3	12
	8%	50%	8%	8%	25%	100%

4. Vertical structure of the SV total energy

In addition to the vertically integrated total energy SVs, the vertical structure of the total energy of the first leading SV and its different components are also of interest and are therefore examined in this section. The vertical distribution and variation of the energy at initial and final times for four major subgroups (NI, RI, A and C; results for group B, not shown, are very similar to results for group A) are discussed.

Figure 9 contains the averages of the vertical profiles of the total, kinetic, and potential energy of the first leading SV for NI, RI, A,[1] and C. The initial energy profiles (solid lines in Fig. 9) are multiplied by 10 to facilitate comparison with the final profiles (dashed lines in Fig. 9). Overall, the total energy at final time is dominated by the kinetic energy. The total energy at initial time is roughly equally composed of kinetic and potential energy. For group NI of the inward flow group, the initial SV total energy maximum occurs at mid-tropospheric levels (500–350 hPa; Fig. 9a), with the kinetic energy maximum between 600–500 hPa (Fig. 9b) and the potential energy maximum at 400–300 hPa (Fig. 9c). At final time, the SV maximum occurs near 600 hPa, which is dominated by the kinetic energy component (Figs. 9a,b). Thus, for the group NI, the energy maximum shifts from middle to lower levels between initial and final times. For the group RI, the initial SV total energy peaks at 450 hPa (Fig. 9d), with the larger contribution coming from the potential energy component (Fig. 9f). At final time, the total energy maximum occurs at 300 hPa (Fig. 9d) and is dominated by the kinetic energy component (Fig. 9e). Therefore, for the group RI, the total energy maximum shifts slightly from a middle level to higher levels and from the potential to the kinetic component from initial to final time. This may reflect the fact that the final energy in the verification domain may catch part of the upper-level jet in the initial SV, and the changes to the trough at initial time will affect both the trough and the TC at final time.

Similar to group NI, the initial and final SV total energy maxima of group A are located around 400 and 600 hPa, respectively (Fig. 9g). The final total energy is mainly composed of the kinetic energy component. At the initial time, the potential energy component is maximal at 400–350 hPa, whereas the kinetic energy component maximum occurs at about 600 hPa (Figs. 9g–i). The features of the total energy profile and the relative contributions of the two energy components of group C (Figs. 9j–l) are similar to those of group RI (Figs. 9d–f). Group C shows the shift in total energy maximum from the middle to upper levels (Figs. 9j–l).

In summary, groups NI and A have the largest total energy in the lower part of the atmosphere (below 400 hPa), whereas groups RI and C have the largest total energy in the upper part of the atmosphere.

5. Summary and discussion

This study uses NOGAPS SVs to investigate the dynamical features associated with TC evolution for the western North Pacific Ocean in 2006. The SVs are constructed from the dry tangent linear and adjoint models of NOGAPS that are linearized with respect to the full-physics, nonlinear, high-resolution global forecasts. The leading SVs represent the fastest-growing perturbations (in a linear sense) about the forecast trajectory. For the 72 TC forecasts from this season, SVs are calculated to optimize the perturbation energy growth in a $20° \times 20°$ box centered on the final-time forecast position of the TC over a 2-day optimization period using a local projection operator. The initial SVs indicate where the 2-day TC forecast is most sensitive to changes in the initial analysis and therefore can be used to understand the dynamics associated with the TC evolution.

From the synoptic analysis of the typhoon season in 2006, it can be found that the TC tracks are consistent with the environmental flow associated with the large-scale systems. Moreover, in the western North Pacific, the large-scale environmental flow is dominated by the seasonal evolution in the Asian monsoon and the strength and the location of the subtropical high. The evolution of these fields leads to the subseasonal variation of the steering flow of the TCs. Hence, the TCs show different track characteristics in the different periods of the typhoon season.

Composites for the 72 cases show that the initial SVs are collocated with regions of flow toward the storm, and

[1] One case (No. 64) is omitted from the group-A profiles due to a spurious energy maximum at 500 hPa that is remote from the TC and not associated with the TC SV signal.

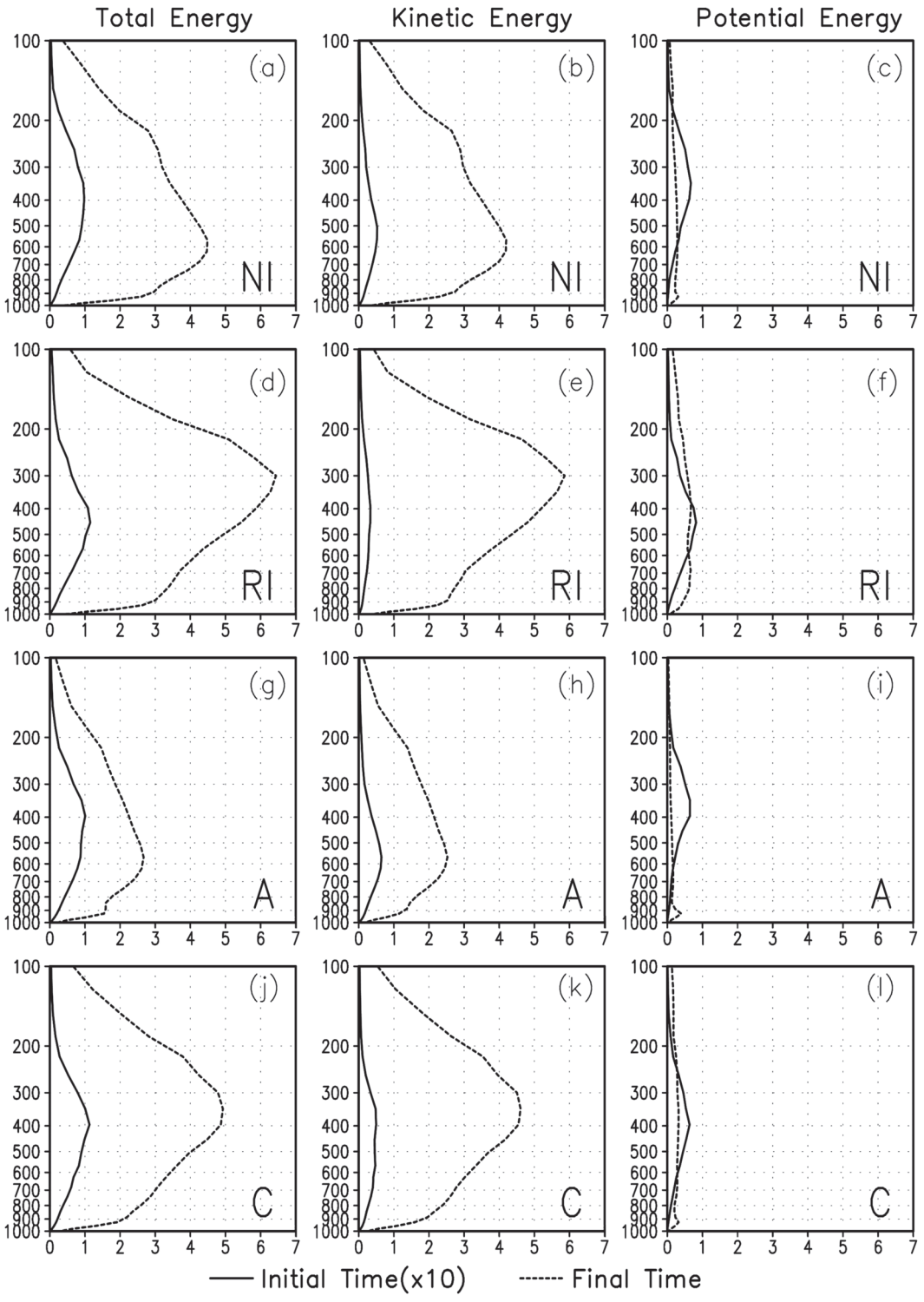

FIG. 9. Vertical profile (pressure coordinate) of the (left) total, (middle) kinetic, and (right) potential energy composites for the leading SV for groups (a)–(c) NI, (d)–(f) RI, (g)–(i) A, and (j)–(l) C. Solid and dashed lines indicate the initial and final times, respectively. The values for the initial time have been multiplied by 10 to facilitate comparison. All the units are J kg^{-1}.

the maximum SV is located at around 500 km from the center, consistent with Peng and Reynolds (2006). Composites of the height and wind fields reveal the subtropical high and the midlatitude trough or jet that have a major influence on the TC evolution. Based on the location of the initial SV maximum with respect to the radial wind field of each case, the 72 cases are classified into two groups: ''inward flow'' and ''low radial wind speed.'' For the inward flow group, the SV maximum is highly collocated with the strong inflow region where U_r is at its negative maximum. This group can be divided into two subgroups: ''near inflow'' (''NI'') and ''remote inflow'' (''RI''). The SV maximum for the subgroup NI is located in the inflow region to the east of the storm and is very close to the storm center (450 km). The primary SV maximum of the RI composite is associated with regions of inward flow located in the northwestern quadrant of the storm with larger distance to the center (1500–2000 km). It is found that most of the NI cases occur in the early typhoon season and have straight-moving tracks associated with the steering flow from the subtropical high. For the RI group, many cases occur in the late typhoon season or late TC development stage and have recurving tracks influenced by the midlatitude jet or trough.

The radial component of the wind field used in this study represents the TC's steering flow qualitatively. It is believed that the SV sensitivity marks the region where the change of inward flow will influence the future track of the TC. For application to targeted observation of TCs, these two SV sensitivity patterns can provide general information on the factors influencing TC evolution. It offers some important and useful guidance for constructing observing strategies for TCs under different environmental backgrounds and in different subseasons.

The second group is composed of the cases in which the SV maxima are within the low-radial-wind-speed area. Some of these low-radial-wind speed areas are within the weak inflow region (with negative U_r, but its absolute value and not the local maximum) and others are located between the inflow and outflow regions, where U_r is close to zero. It is a new and interesting finding, not shown in extant studies, that SVs are not always collocated with strong inflow regions. In this second group, three subgroups (A, B, and C) are classified depending on the location of the SV maximum relative to the storm. In group A, the SV maxima are mainly located to the east of the TC, while the SV maxima are located to the southeast and northwest of the TC in groups B and C, respectively. From the monthly case-number distribution and the synoptic analyses, the subseasonal correlation of the changes of the low-speed radial wind locations and the SV maximum locations are found. In the early typhoon season, the confluence of the circulations of the subtropical high and the TC causes the reduction of the zonal wind, resulting in the low speed of the inward flow to the east side of the storm center. In the middle of the typhoon season, the subtropical high becomes stronger and extends to the east of the TC. The confluence of the subtropical high and the TC circulations shifts to the southeast side of the storm center. The counteraction of the flows from the two systems causes the weak wind in the confluence region and thus the low speed of the radial wind in that area. In the late season, a saddle located to the northwest of the storm is caused by the confluence of the circulations from four systems: the subtropical high, the midlatitude jet, the TC, and a separated high located to the west. At the saddle point, the overall wind speed is low, and the radial wind speed is also consequently low.

At the confluence area, especially the saddle point, the weak steering flow causes difficulty in both subjective and numerical TC track forecasting. In this study, many of the initial SV maxima are shown in the confluence regions that are generated by several systems such as the subtropical high, the midlatitude jet, and the TC itself. It implies that the low-radial-wind-speed areas represent regions with a delicate balance between two or more synoptic systems. A small perturbation locally can be the result of more significant differences of the associated synoptic systems that could lead to very different steering flow and impact the TC evolution.

The total energy vertical profiles of the first leading SV are also examined for the NI, RI, A, and C groups in this study. For the four subgroups, the total energy at final time is dominated by the kinetic energy, whereas it is roughly equally composed of kinetic and potential energy at initial time. For the NI cases, the energy maximum shifts from middle to lower levels between initial and final times. In contrast, the total energy maximum shifts from middle level to high level and from the potential component to kinetic component from initial to final time for the RI group. This may reflect the fact that the final energy in the verification domain may include part of the upper-level jet because changes to the jet or trough at initial time will impact both the TC and the jet at final time. Similar to group NI, the initial and final SV total energy maxima of group A shift from middle to lower levels. Group C shows the shift in total energy maximum from the middle to upper levels, similarly to group RI. In short, for groups NI and A, the total energy occurs primarily in the lower troposphere (below 400 hPa), whereas for groups RI and C the total energy occurs in middle and upper troposphere.

From the NOGAPS SV perspective, several different sensitivity patterns that highlight the relationship between

the TC forecast and the environment in the western North Pacific in 2006 have been shown. This study goes beyond the initial results of Peng and Reynolds (2006), using more specific composites that illustrate the relationship between the TC evolution and the surrounding synoptic-scale features in finer detail, and investigates the subseasonal variation of the relationship between the TC and other synoptic systems. How the subseasonal variation during the typhoon season of 2006 behaves in different years remains to be further investigated. The collocation of the SV maxima and low-radial-wind-speed regions is one of the most important new findings. Our results show that the SV sensitivities have the ability to represent the distinct dynamical characteristics associated with TC evolution in different subseasons or during different stages of the TC life cycle. These sensitivities may be induced by the interaction between the TC itself and the synoptic systems at different orientations and locations relative to the storm in different subseasons. The connection between the NOGAPS SVs and these synoptic systems suggest that the SVs can provide useful guidance for targeted TC observation programs. In fact, NOGAPS SVs have already been employed for this purpose in recent field programs, such as DOTSTAR (Wu et al. 2005), Typhoon Hunting 2008 (TH08), and Tropical Cyclone Structure–2008 (TCS-08) in THORPEX-PARC (T-PARC; Elsberry and Harr 2008).

Acknowledgments. The work is supported by the National Science Council of Taiwan through Graduate Students Study Abroad Program (Grant NSC96-2917-I-002-004) and Grant NSC95-2119-M-002-039-MY2, the Office of Naval Research Grants N00014-05-1-0672 and N00173-08-1-G007, and National Taiwan University Grant 97R0302. M. S. Peng and C. A. Reynolds gratefully acknowledge the support of the sponsor, the Office of Naval Research (ONR) through Program Element and 0601153N. The DoD High Performance Computing Program at NAVO MSRC provided part of the computing resources.

REFERENCES

Aberson, S. D., 2002: Two years of hurricane synoptic surveillance. *Wea. Forecasting,* **17,** 1101–1110.

——, 2003: Targeted observations to improve operational tropical cyclone track forecast guidance. *Mon. Wea. Rev.,* **131,** 1613–1628.

——, and M. DeMaria, 1994: Verification of a nested barotropic hurricane track forecast model (VICBAR). *Mon. Wea. Rev.,* **122,** 2804–2815.

——, and J. L. Franklin, 1999: Impact on hurricane track and intensity forecast of GPS dropsonde observations from the first-season flights of the NOAA Gulfstream-IV jet aircraft. *Bull. Amer. Meteor. Soc.,* **80,** 421–427.

Buizza, R., 1994: Localization of optimal perturbations using a projection operator. *Quart. J. Roy. Meteor. Soc.,* **120,** 1647–1681.

——, and A. Montani, 1999: Targeting observations using singular vectors. *J. Atmos. Sci.,* **56,** 2965–2985.

Burpee, R. W., J. L. Franklin, S. J. Lord, R. E. Tuleya, and S. D. Aberson, 1996: The impact of omega dropwindsondes on operational hurricane track forecast models. *Bull. Amer. Meteor. Soc.,* **77,** 925–933.

Chan, J. C. L., and W. M. Gray, 1982: Tropical cyclone movement and surrounding flow relationships. *Mon. Wea. Rev.,* **110,** 1354–1374.

——, and R. T. Williams, 1987: Analytical and numerical studies of the beta-effect in tropical cyclone motion. Part I: Zero mean flow. *J. Atmos. Sci.,* **44,** 1257–1265.

Elsberry, R. L., 1986: Some issues related to the theory of tropical cyclone motion. Naval Postgraduate School Tech. Rep. NPS 63-86-005, 23 pp.

——, and P. A. Harr, 2008: Tropical cyclone structure (TCS08) field experiment science basis, observational platforms, and strategy. *Asia.–Pac. J. Atmos. Sci.,* **44,** 209–231.

Farrell, B. F., 1990: Small error dynamics and the predictability of atmospheric flows. *J. Atmos. Sci.,* **47,** 2409–2416.

Fiorino, M., and R. L. Elsberry, 1989: Some aspects of vortex structure related to tropical cyclone motion. *J. Atmos. Sci.,* **46,** 975–990.

Gray, W. M., 1975: Tropical cyclone genesis. Dept. of Atmospheric Science Paper 232, Colorado State University, 121 pp.

Hanley, D., J. Molinari, and D. Keyser, 2001: A composite study of the interactions between tropical cyclones and upper-tropospheric troughs. *Mon. Wea. Rev.,* **129,** 2570–2584.

Joly, A., and Coauthors, 1997: The Fronts and Atlantic Storm-Track Experiment (FASTEX): Scientific objectives and experimental design. *Bull. Amer. Meteor. Soc.,* **78,** 1917–1940.

Kim, H. M., and B.-J. Jung, 2008: Singular vector structure and evolution of a recurving tropical cyclone. *Mon. Wea. Rev.,* **137,** 505–524.

Langland, R. H., R. Gelaro, G. D. Rohaly, and M. A. Shapiro, 1999: Targeted observations in FASTEX: Adjoint-based targeting procedures and data impact experiments in IOP 17 and IOP 18. *Quart. J. Roy. Meteor. Soc.,* **125,** 3241–3270.

Lorenz, E. N., 1965: A study of the predictability of a 28-variable atmospheric model. *Tellus,* **17,** 321–333.

Majumdar, S. J., S. D. Aberson, C. H. Bishop, R. Buizza, M. S. Peng, and C. A. Reynolds, 2006: A comparison of adaptive observing guidance for Atlantic tropical cyclones. *Mon. Wea. Rev.,* **134,** 2354–2372.

McBride, J. L., and R. Zehr, 1981: Observational analysis of tropical cyclone formation. Part II: Comparison of non-developing versus developing systems. *J. Atmos. Sci.,* **38,** 1132–1151.

Molinari, J., P. Dodge, D. Vollaro, K. L. Corbosiero, and F. Marks Jr., 2006: Mesoscale aspects of the downshear reformation of a tropical cyclone. *J. Atmos. Sci.,* **63,** 341–354.

Molteni, F., and T. N. Palmer, 1993: Predictability and finite-time instability of the northern winter circulation. *Quart. J. Roy. Meteor. Soc.,* **119,** 269–298.

——, R. Buizza, T. N. Palmer, and T. Petroliagis, 1996: The ECMWF ensemble prediction system: Methodology and validation. *Quart. J. Roy. Meteor. Soc.,* **122,** 73–120.

Palmer, T. N., R. Gelaro, J. Barkmeijer, and R. Buizza, 1998: Singular vectors, metrics, and adaptive observations. *J. Atmos. Sci.,* **55,** 633–653.

Peng, M. S., and C. A. Reynolds, 2005: Double trouble for typhoon forecasters. *Geophys. Res. Lett.,* **32,** L02810, doi:10.1029/2004GL021680.

——, and ——, 2006: Sensitivity of tropical cyclone forecasts as revealed by singular vectors. *J. Atmos. Sci.,* **63,** 2508–2528.

——, R. N. Maue, C. A. Reynolds, and R. H. Langland, 2007: Hurricanes Ivan, Jeanne, Karl (2004) and mid-latitude trough interactions. *Meteor. Atmos. Phys.,* **97,** 221–237.

Reynolds, C. A., M. S. Peng, S. J. Majumdar, S. D. Aberson, C. H. Bishop, and R. Buizza, 2007: Interpretation of adaptive observing guidance for Atlantic tropical cyclones. *Mon. Wea. Rev.,* **135,** 4006–4029.

——, ——, and J.-H. Chen, 2009: Recurving tropical cyclones: singular vector sensitivity and downstream impact. *Mon. Wea. Rev.,* **137,** 1320–1337.

Rosmond, T. E., 1997: A technical description of the NRL adjoint modeling system. NRL Tech. Rep. NRL/MR/7532/97/7230, 53 pp.

Velden, C. S., and L. M. Leslie, 1991: The basic relationship between tropical cyclone intensity and the depth of the environmental steering layer in the Australian region. *Wea. Forecasting,* **6,** 244–253.

Wang, Y., and C.-C. Wu, 2004: Current understanding of tropical cyclone structure and intensity changes—A review. *Meteor. Atmos. Phys.,* **87,** 257–278.

Wu, C.-C., 2006: Targeted observation and data assimilation for tropical cyclone track prediction. *Proc. Sixth Int. Workshop on Tropical Cyclones,* San Jose, Costa Rica, WMO, 409–423.

——, and K. A. Emanuel, 1993: Interaction of a baroclinic vortex with background shear: Application to hurricane movement. *J. Atmos. Sci.,* **50,** 62–76.

——, and ——, 1995a: Potential vorticity diagnostics of hurricane movement. Part I: A case study of Hurricane Bob (1991). *Mon. Wea. Rev.,* **123,** 69–92.

——, and ——, 1995b: Potential vorticity diagnostics of hurricane movement. Part II: Tropical Storm Ana (1991) and Hurricane Andrew (1992). *Mon. Wea. Rev.,* **123,** 93–109.

——, T.-S. Huang, W.-P. Huang, and K.-H. Chou, 2003: A new look at the binary interaction: Potential vorticity diagnosis of the unusual southward movement of Typhoon Bopha (2000) and its interaction with Supertyphoon Saomai (2000). *Mon. Wea. Rev.,* **131,** 1289–1300.

——, and Coauthors, 2005: Dropwindsonde Observations for Typhoon Surveillance near the Taiwan Region (DOTSTAR): An overview. *Bull. Amer. Meteor. Soc.,* **86,** 787–790.

——, J.-H. Chen, P.-H. Lin, and K.-H. Chou, 2007a: Targeted observations of tropical cyclone movement based on the adjoint-derived sensitivity steering vector. *J. Atmos. Sci.,* **64,** 2611–2626.

——, K.-H. Chou, P.-H. Lin, S. D. Aberson, M. S. Peng, and T. Nakazawa, 2007b: The impact of dropwindsonde data on typhoon track forecasts in DOTSTAR. *Wea. Forecasting,* **22,** 1157–1176.

——, S.-G. Chen, J.-H. Chen, K.-H. Chou, and P.-H. Lin, 2009a: Interaction of Typhoon Shanshan (2006) with the midlatitude trough from both adjoint-derived sensitivity steering vector and potential vorticity perspectives. *Mon. Wea. Rev.,* **137,** 852–862.

——, and Coauthors, 2009b: Intercomparison of targeted observation guidance for tropical cyclones in the western North Pacific. *Mon. Wea. Rev.,* **137,** 2471–2492.

Yamaguchi, M., T. Iriguchi, T. Nakazawa, and C.-C. Wu, 2009: An observing system experiment for Typhoon Conson (2004) using a singular vector method and DOTSTAR data. *Mon. Wea. Rev.,* **137,** 2801–2816.

Yang, C.-C., C.-C. Wu, K.-H. Chou, and C.-Y. Lee, 2008: Binary interaction between Typhoons Fengshen (2002) and Fungwong (2002) based on the potential vorticity diagnosis. *Mon. Wea. Rev.,* **136,** 4593–4611.